Shock Waves (2005)
Digital Object Identifier (DOI) 10.1007/s00193-005-0244-y

Shock Waves

Original article

Abel inversion of axially-symmetric shock wave flows

A.F.P. Houwing[1], K. Takayama[2], Z. Jiang[3], T. Hashimoto[2], K. Koremoto[2], H. Mitobe[2], M.J. Gaston[4]

[1] ALDiR Laboratory, Department of Physics, Faculty of Science, Australian National University, ACT 0200, Australia (e-mail: Frank.Houwing@anu.edu.au)
[2] Shock Wave Research Center, Institute of Fluid Science, Tohoku University, Sendai, Aoba 980-8577, Japan
[3] Laboratory of High Temperature Gas Dynamics, Institute of Mechanics, Chinese Academy of Sciences, No. 15 Beisihuanxi Road, Beijing, China (100080)
[4] Faculty of Engineering, University of Technology, Sydney, Broadway, NSW, 2007, Australia

Received 12 November 2003 / Accepted 21 October 2004
Published online 31 March 2005 –
Communicated by R. Boyce

Abstract. Finite-fringe interferograms produced for axisymmetric shock wave flows are analyzed by Fourier transform fringe analysis and an Abel inversion method to produce density field data for the validation of numerical models. For the Abel inversion process, we use basis functions to model phase data from axially-symmetric shock wave structure. Steady and unsteady flow problems are studied, and compared with numerical simulations. Good agreement between theoretical and experimental results is obtained when one set of basis functions is used during the inversion process, but the shock front is smeared when another is used. This is because each function in the second set of basis functions is infinitely differentiable, making them poorly-suited to the modelling of a step function as is required in the representation of a shock wave.

Key words: Abel, inversion, basis, functions
PACS: 47.40.-x, 42.40.Kw, 02.30.Zz

1 Introduction

As described by Takayama [1] and Houwing et al. [2], holographic interferometry can be used to study a variety of high speed flow problems of interest to physicists and engineers. In particular, it is a powerful experimental technique for producing quantitative data against which computational fluid dynamic (CFD) models can be verified or validated.

In the case of two-dimensional flows, comparisons between CFD and experiment are reasonably straightforward, since fringes in infinite-fringe interferograms correspond directly to density contours.

In the case of axisymmetric or three-dimensional flows, this is not true and a direct comparison between theoretical and experimental density is no longer possible, although Boyce et al. [3] show that post-processing of CFD results can be used to produce theoretical phase maps against which experimental phase data can be compared.

In the special case of axisymmetric flows, with which the current work is concerned, Abel deconvolution as described by Bracewell [4] can be used, but this often involves computationally-intensive numerical integration to produce the required density field. For certain Abel transforms, however, numerical integration is unnecessary during deconvolution because their inverse transforms can be determined analytically. Such Abel transforms and their inverse functions are provided by [4]. In the current work, we use these transforms as basis functions in a vector representation of the experimental phase data, whereas their corresponding inverse transforms are used as basis functions in a vector representation of the deconvoluted density. This allows us to recover the axially-symmetric density field in a straight-forward manner by determining the components of these vectors through a least square fit of the theoretical phase vector to the experimental phase data. Furthermore, we shall demonstrate that the basis functions we select can resolve the discontinuous density jump across shock waves, whereas power law basis functions result in this jump being smeared. A further aim of our work is to show that the basis function inversion method produces experimental data suitable for CFD validation. To fulfil these objectives we performed two experiments as described below.

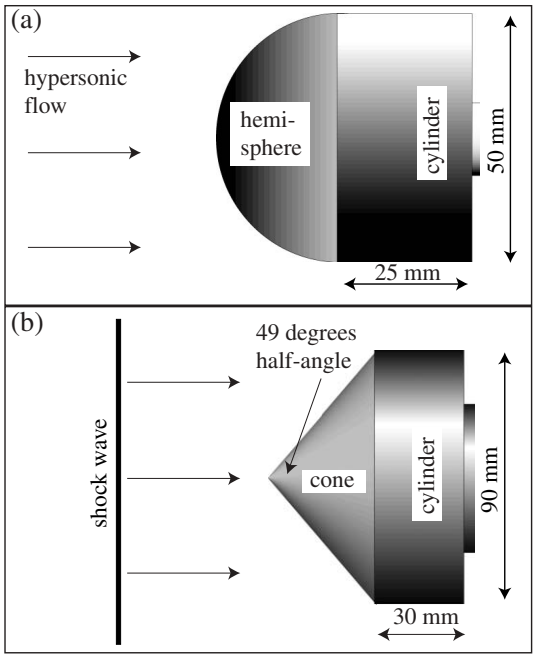

Fig. 1. Schematics of **a** steady axisymmetric shock layer flow experiment and **b** unsteady axisymmetric shock reflection experiment

2 The experiments

Two different axisymmetric flow problems were studied. One was a steady hypersonic flow incident upon a stationary axisymmetric body, as illustrated in Fig. 1(a). The other was an unsteady flow produced by the reflection of a shock wave over a cone, as illustrated in Fig. 1(b).

2.1 Experimental facilities and test conditions

The steady flow experiment was performed in the hypersonic stream produced by a free-piston shock tunnel as described by Koremoto [5]. The axisymmetric body used was a spherically-blunted cylinder with a diameter of 50 mm, whose axis was aligned with the axis of symmetry of the incident flow. The model was placed centrally within the inviscid core flow downstream of the nozzle of the shock tunnel. The nozzle was conical with an exit diameter of 130 mm, whereas the inviscid core flow at the location of the model was estimated from Pitot pressure measurements by Koremoto [5] to be approximately 100 mm in diameter. For the unsteady flow experiment, a diaphragmless shock tube as described by Mitobe [6], with a 100 mm $\times$ 180 mm rectangular cross-section, was used. In this case, the axisymmetric model was a cone with a base diameter of 90 mm, a half-angle of 49°, and whose axis of symmetry was aligned with the direction of propagation of the incident shock

2.2 Test conditions for steady flow experiment

The freestream conditions for the steady flow experiment are given in Table 1. The conditions at the exit of the nozzle were determined by the computer code STUBE written by Vardavas [7] using the measured primary shock speed and the nozzle reservoir pressure as input. Based on the uncertainties in the measured values, the uncertainty in the calculated values given in Table 1 are estimated to be $\pm$ 5%. The test gas was partially dissociated air, for which the mass fractions were calculated by STUBE to be 67% N_2, 13% O_2, 1% Ar and 19% NO. The theoretical calculations used in the current work assume that the flow remains in thermal equilibrium during the expansion through the shock tunnel's nozzle. Based on this assumption, the code determines the flow at the exit of the nozzle to have an effective ratio of specific heats of 1.33. Having said this, it is important to note that Palma et al. [8] show that the rotational and vibrational temperatures differ significantly in the hypersonic nozzle flows of free-piston shock tunnels. Hence, the assumption of thermal equilibrium is expected to result in systematic errors in the calculated flow conditions. However a determination of the influence of these effects on the steady flow problem are beyond the scope of the current work and must be postponed to future consideration.

Table 1. Freestream conditions for steady flow experiment

T_∞ (K)	p_∞ (kPa)	u_∞ (km/s)	ρ_∞ (kg/m^3)	M_∞
387	2.26	2.75	0.02	7.1

Table 2. Initial conditions for unsteady flow experiment

T_1 (K)	p_1 (kPa)	M_S
292	14.1	2.33

2.3 Test conditions for unsteady flow experiment

The initial conditions for the unsteady flow experiment are shown in Table 2. The incident shock Mach number was determined by measuring the shock transit time between transducers upstream of the model. The pressure and temperature ahead of the incident shock were measured as described by Mitobe [6]. The errors in these measured values are less than 1%, and the flow conditions were such that perfect gas behavior, with a ratio of specific heats of 1.4, can be assumed. However, viscous effects are expected to play a role in the reflection process.

3 Numerical methods

As stated in Sect. 1, one of the purposes of our work is to show how the experimental density information produced by our deconvolution method can be used to test computational fluid dynamics (CFD) simulations.

For the two different flow problems studied here, we used two different CFD methods. For the steady flow

problem, we used the compressible flow solver, CFD-FASTRAN^{TM} [9], and assumed inviscid perfect gas flow with a ratio of specific heats $\gamma = 1.33$.

For the unsteady flow problem, the numerical technique devised by Jiang [10] was used. His computational scheme meets the dispersion conditions described by Jiang et al. [11], which make it possible to capture a discontinuity without any numerical oscillations, and without requiring artificial viscosity.

3.1 Finite-fringe holographic interferometry

In our work, a double-exposure finite-fringe holographic interferometry system is used. This system and the fringe analysis method used to recover phase data from finite-fringe interferograms are discussed by Houwing et al. [2]. The details will not be repeated here.

3.2 Determination of density from the phase data

For an axially-symmetric flow, the projected phase $\phi(y,z)$ for each line-of-sight perpendicular to the axis of symmetry is given by,

$$\phi(y,z) - \phi_{\rm ref} = \frac{2\pi}{\lambda}\int [n_{\rm ref} - n_{\rm flow}(\sqrt{x^2+y^2},z)]dx \ , \quad (1)$$

where λ is the wavelength of light and n is the refractive index. The subscripts 'ref' and 'flow' refer to 'reference' and 'flow' conditions, respectively. In the above equation, x, y and z are coordinates in an xyz Cartesian coordinate system, where x in the direction of the line-of-sight and z is along the axis of symmetry. Because of the axial symmetry, the flow properties depend only on the values of z and $r = \sqrt{y^2+z^2}$, where r and z are the radial and axial coordinates respectively, in a cylindrical polar coordinate system. The integral in Eq. (1) is the Abel transform of $\frac{2\pi}{\lambda}\left[n_{\rm ref} - n_{\rm flow}\left(r,z\right)\right]$.

Following Bracewell [4], the inverse Abel transform can be used to write the radial distribution of the refractive index in terms of the projected phase:

$$n_{\rm ref} - n_{\rm flow}(r,z) = \frac{-\lambda}{2\pi^2}\int_r^\infty [\frac{1}{\sqrt{y^2-r^2}}\frac{d\phi(y,z)}{dy}]dy \ . \quad (2)$$

In general, the above form can be used to determine the refractive index and, ultimately, the density, to which it is proportional, by numerical integration. However, in the current work, we make use of basis functions to avoid such numerical integration. This is more desirable because it avoids the numerical evaluation of the derivative $\frac{d\phi(y,z)}{dy}$ in Eq. (2), which we found contributes to numerical noise during the inversion process. For a perfect gas of uniform composition, the refractive index can be related directly to the density, ρ, of the gas and its value at a standard density, ρ_s, as described by Liepmann and Roshko [12]:

$$n = 1 + \beta\frac{\rho}{\rho_s} \ . \quad (3)$$

Values for β and ρ_s for the gases used in the current work are available in the same reference.

In general, by using Eqs. (3) and (2), it is possible to determine the radial density distribution. In our approach, the experimental phase data is modelled by a linear combination of basis functions for which the analytic solutions to Eq. (2) are known. In the current work, we refer to this linear combination as a vector representation of the phase data. Once the phase data has been modelled in this way, the density can be readily determined by a linear combination of the corresponding inverse functions, with the same coefficient being used for each basis function and its corresponding inverse. We have found this approach to be a more efficient and more accurate way of performing the deconvolution than through direct numerical evaluation of the integral in Eq. (2).

We have found that the choice of basis functions is very important, with the suitability of any particular basis determined by two properties: (i) the overlap (inner product) of each basis function with the object in question; and (ii) the difference (orthogonality) of each basis function with each other basis function. The first property ensures that the basis has common features with the object, and the second property ensures that each basis function is sufficiently different so as to be able to resolve as many of the object features as possible. From these considerations, we have chosen five of the functions provided by [4] as being suitable for modelling shock waves. In the current work, we refer to these as 'well-suited' basis functions. We now describe how we can make use of these functions to determine the density distribution in axisymmetric shock wave flows.

First, we assume that the refractive index distribution, $n_{\rm flow}(r,z) - n_{\rm ref}$, can be described by a function $f\left(r,z\right)$, which is equal to a linear combination of basis functions, $f_i\left(r,z\right)$:

$$f\left(r,z\right) = \sum_i c_i\left(z\right) f_i\left(r,z\right) \ , \quad (4)$$

where $c_i\left(z\right)$ are fitting coefficients for a particular axial location z and where the basis functions $f_i\left(r,z\right)$ depend also on the value of z.

The integral of the refractive index along the line of sight is then given by

$$f_A\left(y,z\right) = \sum_i c_i\left(z\right) f_{A,i}\left(y,z\right) \ , \quad (5)$$

where $f_{A,i}\left(y,z\right)$ are the Abel transforms of the basis functions $f_i\left(r,z\right)$. The five *"well-suited basis functions"*, $f_1\left(r,z\right),\ldots,f_5\left(r,z\right)$ selected from [4] are defined below:

$$f_1\left(r,z\right) = \Pi\left(r/2a(z)\right) \ ; \quad (6)$$

$$f_2\left(r,z\right) = \left(a(z)^2 - r^2\right)^{-\frac{1}{2}}\Pi\left(r/2a(z)\right) \ ; \quad (7)$$

$$f_3\left(r,z\right) = \left(a(z)^2 - r^2\right)^{\frac{1}{2}}\Pi\left(r/2a(z)\right) \ ; \quad (8)$$

$$f_4\left(r,z\right) = \left(a(z)^2 - r^2\right)\Pi\left(r/2a(z)\right) \ ; \quad (9)$$

$$f_5\left(r,z\right) = \left(a(z)^2 - r^2\right)^{\frac{3}{2}}\Pi\left(r/2a(z)\right) \ ; \quad (10)$$

where $a(z)$ is the radial position of the shock for a given value of z and

$$\Pi(\zeta) = 1 \text{ for } |\zeta| < \frac{1}{2} \tag{11}$$

and

$$\Pi(\zeta) = 0 \text{ for } |\zeta| \geq \frac{1}{2} \tag{12}$$

The Abel transforms, $f_{A,1}(y,z), \ldots, f_{A,5}(y,z)$, of these functions are:

$$f_{A,1}(y,z) = 2\left(a(z)^2 - y^2\right)^{\frac{1}{2}} \Pi\left(y/2a(z)\right) \; ; \tag{13}$$

$$f_{A,2}(y,z) = \pi \Pi\left(y/2a(z)\right) \; ; \tag{14}$$

$$f_{A,3}(y,z) = \frac{1}{2}\pi\left(a(z)^2 - y^2\right) \Pi\left(y/2a(z)\right) \; ; \tag{15}$$

$$f_{A,4}(y,z) = \frac{4}{3}\left(a(z)^2 - y^2\right)^{\frac{3}{2}} \Pi\left(y/2a(z)\right) \; ; \tag{16}$$

$$f_{A,5}(y,z) = \frac{3\pi}{8}\left(a(z)^2 - y^2\right)^2 \Pi\left(y/2a(z)\right) \; . \tag{17}$$

Using Eq. (1), the coefficients $c_i(z)$ and the value of $a(z)$ at each value of z are determined by fitting the phase to the experimentally determined phase distribution, $\phi(y,z) - \phi_{\text{ref}}$, according to the equation:

$$f_A(y,z) = \frac{\lambda}{2\pi}\left[\phi(y,z) - \phi_{\text{ref}}\right] \; . \tag{18}$$

The values of $c_i(z)$ and $a(z)$ are determined by treating them as free parameters in a least squares fitting routine that minimizes the value of
$\sum_j \left(f_A(y_j,z) - \frac{\lambda}{2\pi}\left[\phi(y_j,z) - \phi_{\text{ref}}\right]\right)^2$,
where the summation is over the fitted data points for a given value of z. Once these values are determined, $f(r,z)$ can be evaluated from Eq. (4), and the density is given by

$$\rho(r,z) = \frac{\rho_s}{\beta} f(r,z) + \rho_{\text{ref}} \; . \tag{19}$$

4 Experimental results and discussion

4.1 Interferograms

Finite fringe interferograms produced in the two experiments are shown in Figs 2 and 3. The interferogram in Fig. 2 shows a continuous fringe shift across the shock even though the density is expected to rise discontinuously at its location. This is a consequence of the gradual increase in the optical path length with z.

Figure 3 shows a portion of an interferogram for shock reflection at the surface of the cone. In this figure, the fringe shift at the top right corner of the interferogram is due to the incident shock wave, which has almost arrived at the shoulder of the cone at the time of the second exposure of the hologram. A slipstream discontinuity can be observed downstream of the triple point. The reflected shock wave is the dominant feature in this interferogram and can be seen extending from the triple point to a region in front of the cone. Like Fig. 2, this interferogram shows a gradual increase in fringe across the shock, again because of the gradual increase in the optical path length with z.

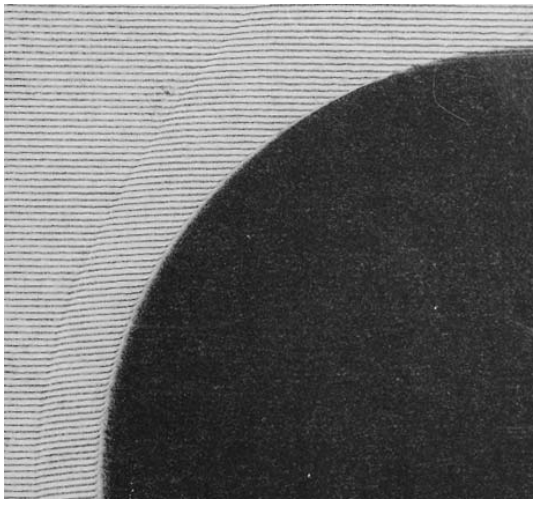

Fig. 2. A portion of an interferogram of hypersonic flow over a spherically-blunted cylinder (from the steady flow experiment). The diameter of the hemispherical forebody is 50 mm

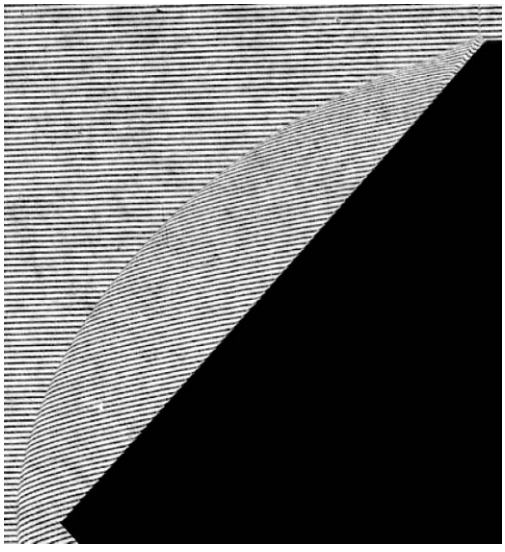

Fig. 3. A portion of an interferogram of shock reflection flow over a cone (from the unsteady flow experiment). The base diameter of the cone is 90 mm

4.2 Deconvolution with ill-suited basis functions

To demonstrate the importance of choosing appropriate basis functions for the deconvolution process, we compare the results obtained by using the well-suited basis functions against results produced by using power-law basis functions. This was achieved by fitting a fifth-order polynomial to the phase, using numerical integration to de-

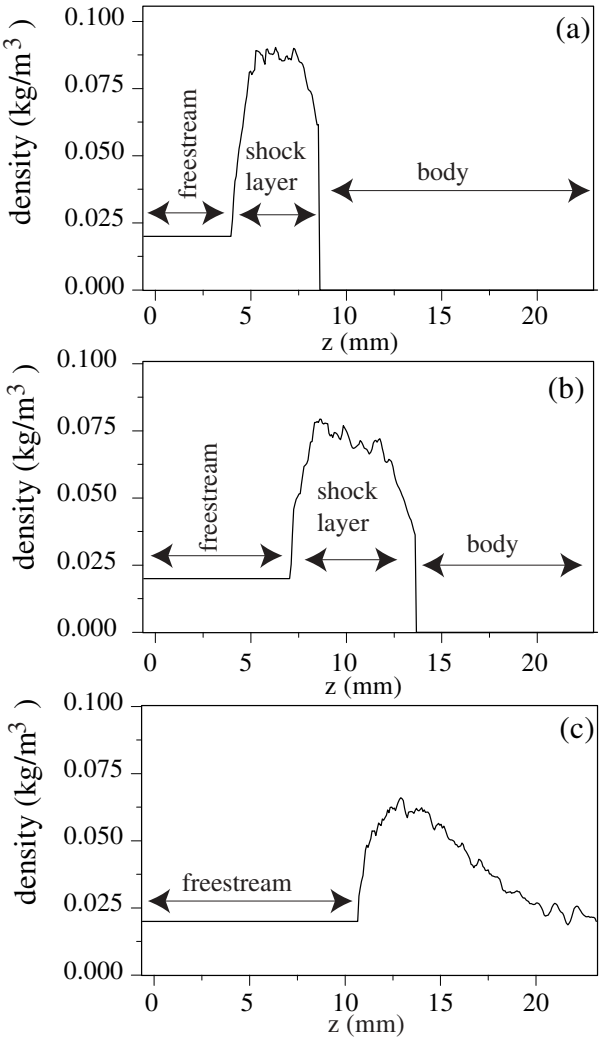

Fig. 4. Profiles of density obtained using power-law basis functions for the steady flow case: **a** $r = 15$ mm; **b** $r = 20$ mm; **c** $r = 25$ mm

termine the refractive index from Eq. (2) and then using Eq. (3) to determine the density.

Density profiles produced from analyzing the steady flow in this manner are shown in Fig. 4. In these profiles, one can observe the density jumps across the shock waves as well as the density changes associated with expansion waves, indicating that the method has revealed the essential qualitative features of the flow behind a curved shock on a bluff body. However, the method has not been entirely successful in producing the steep density jump across the shock wave. The power-law-based deconvolution has 'smeared' the shock wave. This is because power-law basis functions are infinitely differentiable, making them poorly-suited to the modelling of step functions.

4.3 Deconvolution with well-suited basis functions

To determine the flow density using the well-suited basis functions, we first analyzed the interferograms as described by Houwing et al. [2] to produce phase maps and

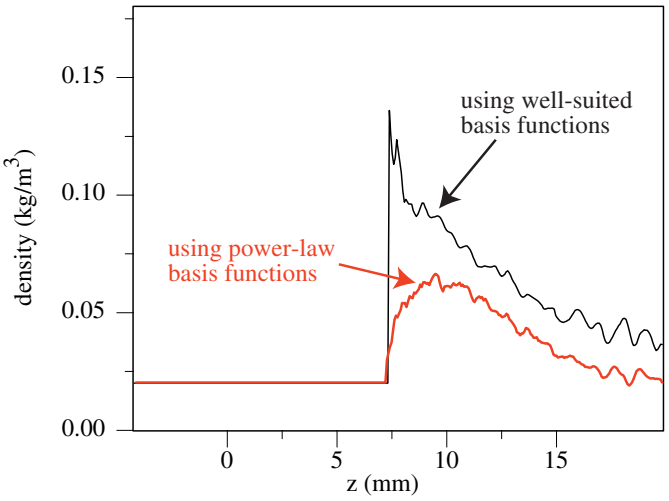

Fig. 5. Comparisons of profiles of density obtained using different basis functions for the steady flow experiment for $r = 25$ mm

then analyzed the phase data as described in Sect. 3.2 The first step in analyzing the phase data involved fitting the function $f_A(r, z)$ given in Eq. (5) to the experimental phase data, so that Eq. (18) was satisfied. This was accomplished through the application of a least-squares fitting algorithm, which provided the values of the coefficients $c_i(z)$, that appear in Eq. (5). Once these coefficients were determined, they were substituted into Eq. (4) to provide values for $f(r, z)$, that were subsequently substituted into Eq. (19), to produce values for the density.

4.4 Comparison of deconvolutions using different basis functions

Figure 5 compares a density profile obtained using the power-law basis functions with one obtained using the well-suited basis functions for the hypersonic flow over the spherically-blunted cylinder. From this comparison, two distinct differences are immediately obvious. Firstly, the inversion using the well-suited basis functions was more successful at reproducing the sharp density rises across the shock than the reconstruction using the power-law basis functions. Secondly, the deconvolution using the well-suited basis functions resulted in larger values for the post-shock density than that using the power-law basis functions.

We believe that these differences are largely due to the fact that the basis function defined in Eq. (13) is ideally-suited to representing the phase shift behind the shock front, it being the Abel transform of the *top-hat* function defined in Eq. (6). The absence of this basis function in the deconvolution using the power-law basis functions means that this deconvolution fails to produce the sharp rise across the shock. It is possible that this difference between the two types of basis functions is responsible for the different density levels behind the shock, however further analysis is required to determine how this is caused.

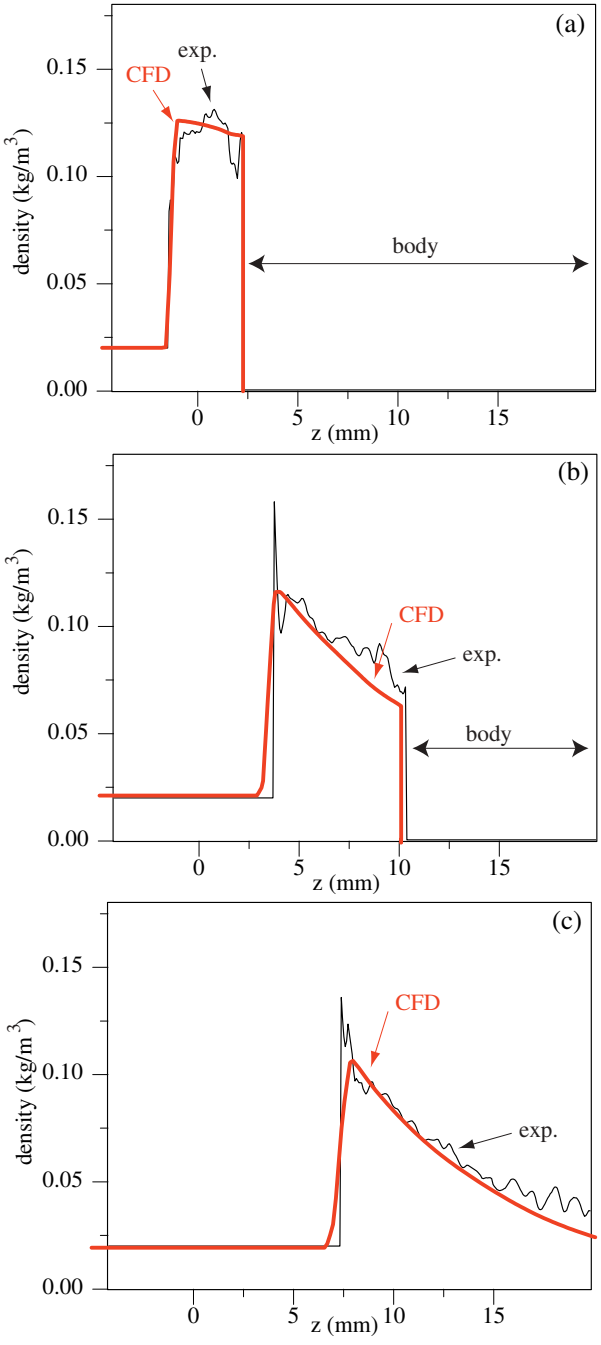

Fig. 6. Steady flow case: density profiles along axial cuts for: **a** $r = 10$ mm; **b** $r = 20$ mm; **c** $r = 25$ mm

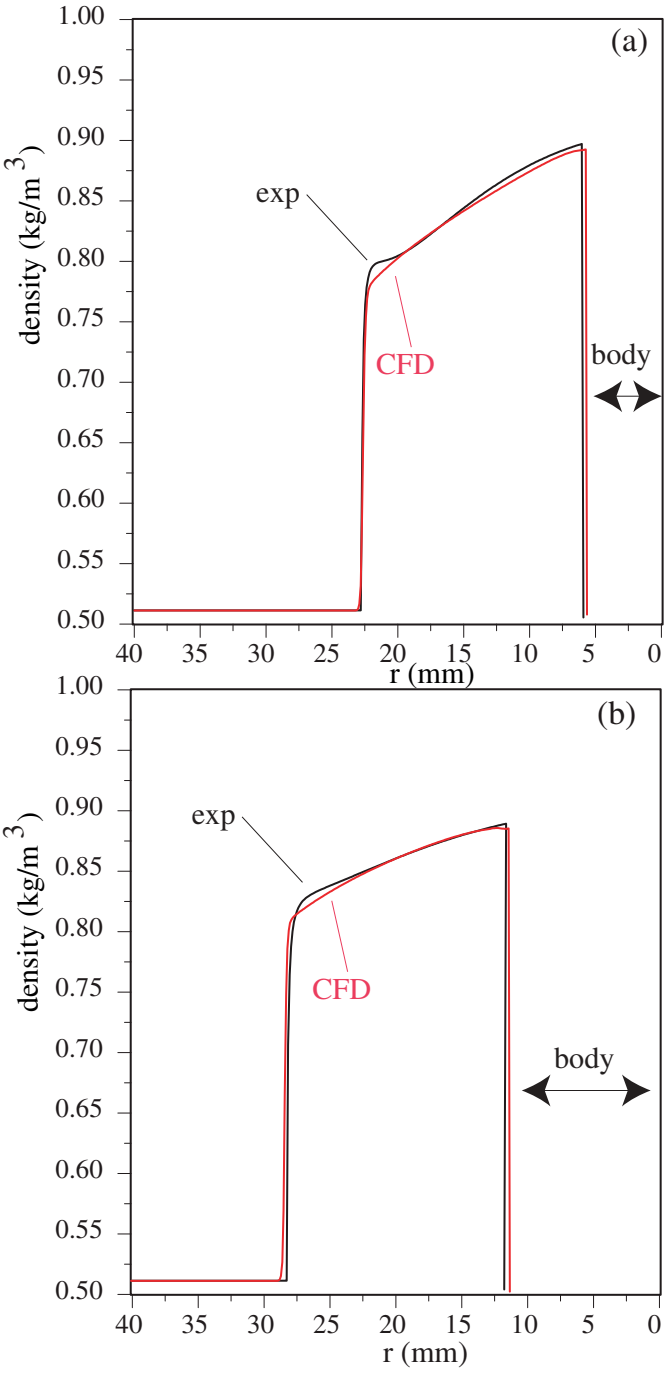

Fig. 7. Unsteady flow case: density profiles along radial cuts for: **a** $z = 5$ mm; **b** $z = 10$ mm

5 Comparison of CFD and experimental results

Figure 6 shows theoretical and experimental density profiles for the steady flow. Profiles are presented for axial cuts at different radial positions. Apart from a very large *overshoot* close to the shock vertex, agreement between theory and experiment is very good. The cut at $r = 10$ mm is close to the stagnation region, where the density is essentially constant. Cuts at $r = 20$ mm and 25 mm are through both the shock wave and the expansion wave near the shoulder of the model, for which the density rises sharply across the shock and decreases continuously through the expansion wave. These trends are observed in both the CFD and experimental results and the CFD code correctly predicts the shock standoff distance from the model surface, providing confidence in the accuracy of the CFD modelling for these conditions. Quantitative agreement between the measured and calculated density is also very good.

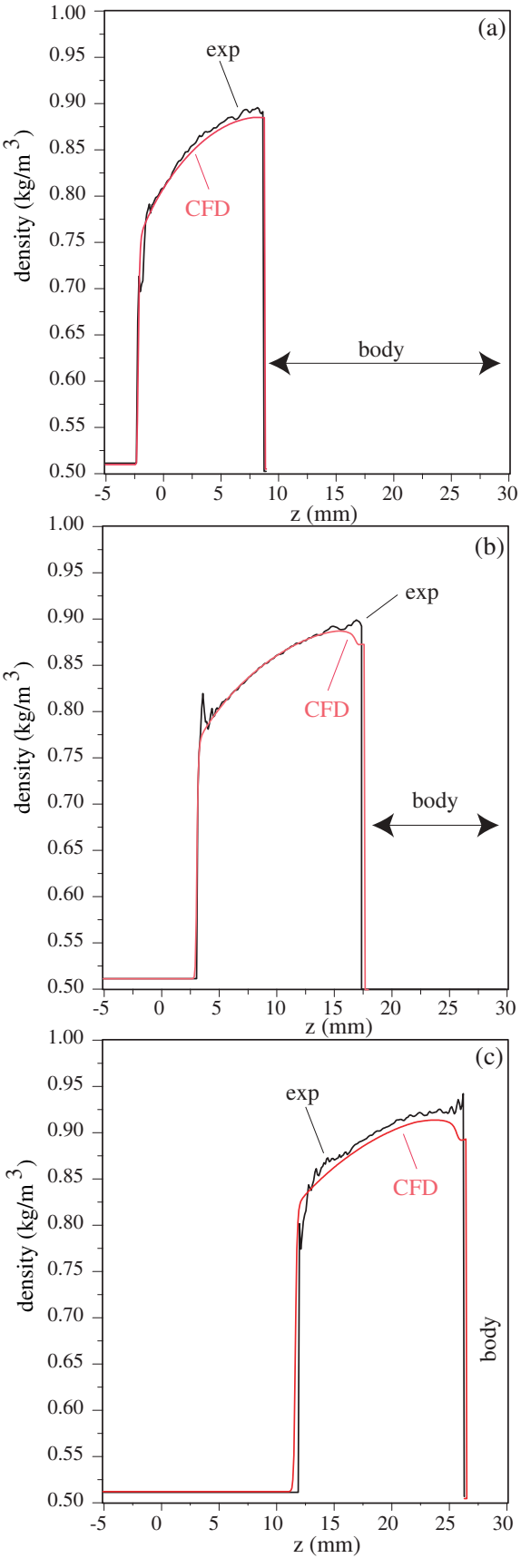

Fig. 8. Unsteady flow case: density profiles along axial cuts for: **a** $r = 10$ mm; **b** $r = 20$ mm; **c** $r = 30$ mm

6 Uncertainties

Based on the uncertainties in the measured primary shock speed and the nozzle reservoir pressure, we expect an uncertainty of approximately ± 10% in the CFD-calculated density distribution for the steady flow case. In contrast, based on the uncertainties in the initial conditions and the measured speed of the incident shock, we expect an uncertainty of approximately ± 5% in the CFD-calculated density distribution for the unsteady flow case. Provided sufficient data points are available for accurate fitting to the phase distribution, and neglecting the overshoot problem close to the shock front, errors from the interferometric measurements of density are estimated to be approximately ±3%. However, within 2 or 3 pixels (less than 1 mm) of the shock front, errors of the order of 100% can sometimes be encountered due to the overshoot problem caused by uncertainties in locating the radial position of the shock, as discussed below.

The overshoot problem occurs near the shock front and is related to the difficulty of fitting the phase accurately close to the shock front, which is in turn related to the uncertainty in locating the radial position $a(z)$ of the shock front. This comes about as follows: The fitting algorithm used in the current work experienced difficulties in iterating towards the best value for the radial position $a(z)$ of the shock. It was found that when $a(z)$ was used as a free parameter in the fitting algorithm, the algorithm failed to converge to a solution for the fitting coefficients. To overcome this problem, we modified the fitting technique so that the shock position was found first. This was achieved by finding the coordinates $(y,\ z)$ in the map of the projected phase $\phi(y, z)$ where the phase changed due to the presence of the shock wave. The coordinates $(y_{\text{shock}},\ z_{\text{shock}})$ effectively locates the shock position in a symmetry plane of the flow, where the shock is at its most-upstream location, that is $(r_{\text{shock}},\ z_{\text{shock}}) = (y_{\text{shock}},\ z_{\text{shock}})$.

Because of the continuous change in the projected phase across a shock in an axisymmetric flow, and because of non-zero noise levels, there will be an error associated with finding the value of $a(z) = r_{\text{shock}}(z)$. This error contributes to errors in the fitted function, with the largest errors occurring within two or three pixels of the shock. These errors will sometimes cause an overshoot in the value of the density at the shock front, however, this overshoot rapidly decays as one moves away from the shock.

For some of the results using the well-suited basis functions, the overshoot at the shock front is particularly large. This is a result of two compounding effects: (i) close to the shock vertex, the number of data points available for fitting through Eq. (18) is small; and (ii) errors in locating the radial position of the near-normal shock wave are larger as one moves closer to the shock vertex. These two effects result in large errors in determining the density directly behind the shock near the shock vertex, often causing a very large overshoot in its value. As one moves away from the shock vertex, the uncertainty in the radial po-

sition of the shock decreases, and this overshoot decays away.

Figure 7 shows comparisons of CFD and experimental density results for the unsteady flow case, showing density profiles along radial cuts for different axial positions. Figure 8 shows comparisons of CFD and experimental density results for the same case, but shows density profiles along radial cuts for different radial positions. As shown in both these figures, agreement between the CFD and experimental results is very good. We estimate the discrepancy to be less than 10% in most parts of the flow. The largest discrepancy is again due to the overshoot problem. However, for these unsteady flow results, the density and hence the fringe shifts are much larger than those in the steady flow results. Hence errors in locating the radial position $a(z)$ of the shock are much less. As a result, the relative magnitudes of errors and overshoots in the unsteady flow case is much less than that in the steady flow case. For both the steady and unsteady flow experiments, the good quantitative agreement between the theoretical and experimental density fields, as well as the good agreement between the theoretical and experimental shock shapes, provides confidence in the accuracy of the CFD modelling.

7 Conclusions

We have demonstrated the use of well-suited basis functions to deconvolute shock wave phase data produced in axisymmetric flows to determine the density in two different flow experiments and compared the results to results using power-law basis functions. In so doing, we have shown that the former method produces better results than the latter, with the former method more successfully resolving the discontinuous density changes across shock waves. Results from CFD simulations have been successfully compared with the experimental results, with the good quantitative agreement giving confidence in the validity of the CFD simulations used.

Acknowledgements. We thank O. Onodera, T. Ogawa and H. Ojima for their technical and professional expertise in assisting to conduct the experiments described in this paper. A.F.P. Houwing gratefully acknowledges the financial support given to him as Visiting Professor at the Shock Wave Research Center at The Institute of Fluid Science at Tohoku University in Sendai to participate in the collaborative research projects described in this paper. The authors gratefully acknowledge the fruitful discussions with R. Faletic on the theory of basis functions.

References

1. Takayama, K.: Application of holographic interferometry to shock wave research. Proc. of the Society of Photo-Optical Instrumentation Engineers **398**, 174–180 (1983)
2. Houwing, A.F.P.,Takayama, K., Jiang, Z., Sun, M., Yada, K., Mitobe, H.: Interferometric measurement of density in nonstationary shock wave reflection flow and comparison with CFD. Shock Waves (in press), DOI 10.1007/s00193-005-0243-z (2005)
3. Boyce, R.R., Morton, J., Houwing, A.F.P., Mundt, C., Bone, D.J.: Computational Fluid Dynamics validation using multiple interferometric views of a hypersonic flowfield. Journal of Spacecraft and Rockets **33**(3), 319–325 (1994)
4. Bracewell, R.N.: The Fourier transform and its applications. McGraw-Hill Book Company, New York, pp. 263–264 (1965)
5. Koremoto, K.: Optimization of the characteristics of a free-piston shock tunnel. PhD Thesis, Tohoku University (1999)
6. Mitobe, H.: Experimental study of the transition from regular reflection to Mach reflection. MSc Thesis, Tohoku University (1999)
7. Vardavas, I.M.: Modelling reactive gas flows within shock tunnels. Australian Journal of Physics **37**, 157–177 (1984)
8. Palma, P.C., Danehy, P.M., Houwing, A.F.P.: Fluorescence imaging of rotational and vibrational temperature in shock-tunnel nozzle flow. AIAA Journal **41**(9), 1722–1732 (2003)
9. CFD-FASTRAN^{TM}:CFD-FASTRAN Tutorials, CFD Research Corporation, Cummings Research Park, 215 Wynn Drive, Huntsville, AL 35805, http://www.cfdrc.com (1999)
10. Jiang, Z.: Study on the finite difference theory and numerical methods of weak solution problems. PhD Thesis, Peking University, Beijing, China (1993)
11. Jiang, Z., Takayama, K., Chen, Y.S.: Dispersion conditions for non-oscillatory shock capturing schemes and its applications. Computational Fluid Dynamics Journal **4**, 137–150 (1995)
12. Liepmann, H.W., Roshko, A.: Elements of Gasdynamics. John Wiley and Sons, New York, p. 154 (1957)